Shock-Bubble Interactions

Devesh Ranjan,[1] Jason Oakley,[2] and Riccardo Bonazza[2]

[1]Department of Mechanical Engineering, Texas A&M University, College Station, Texas 77843; email: dranjan@tamu.edu

[2]Department of Engineering Physics, University of Wisconsin-Madison, Madison, Wisconsin 53706

Keywords

Abstract

When a shock wave propagates through a medium of nonuniform thermodynamic properties, several processes occur simultaneously that alter the geometry of the shock wave and the thermodynamic state of the medium. These include shock compression and acceleration of the medium, refraction of the shock, and vorticity generation within the medium. The interaction of a shock wave with a cylinder or a sphere (both referred to as a bubble in this review) is the simplest configuration in which all these processes take place and can be studied in detail. Shock acceleration leads to an initial compression and distortion of the bubble, followed by the formation of a vortex pair in the two-dimensional (2D) case and a vortex ring in the 3D case. At later times, for appropriate combinations of the incident shock strength and density contrast between the bubble and ambient materials, secondary vortices are formed, mass is stripped away from the original bubble, and mixing of the bubble and ambient fluids occurs.

1. INTRODUCTION

The flow field generated by the interaction of a shock wave with a geometrically well-defined density inhomogeneity involves the strong coupling of several types of fluid dynamic phenomena, including shock-wave refraction and reflection, vorticity production and transport, and turbulence. This interaction results in a complex pattern of shock and rarefaction waves (focusing and scattering), while simultaneously resulting in the formation of characteristic vortices and often enhancing the mixing of the ambient gas with the gas inhomogeneity. This is a problem of fundamental interest, which can be construed as a building block toward the development of an understanding of more complicated problems involving shock propagation through random media characterized by inhomogeneities in density, temperature, or other thermodynamic state variables. The shock-bubble interaction (SBI) is a basic configuration for studying the more general case of shock-accelerated inhomogeneous flows (SAIFs) (Zabusky 1999). In the study of the interaction of a shock wave with a single bubble, analogies may be drawn to the well-known development of the Richtmyer-Meshkov instability of perturbations on impulsively accelerated fluid interfaces (Brouillette 2002).

SAIFs occur in a wide variety of physical situations covering broad ranges of spatial, temporal, and energy scales including, but not limited to, astrophysical flows (Arnett 2000) and, in particular, the interaction of supernova remnants with interstellar clouds (Hwang et al. 2005, Klein et al. 1994), atmospheric sonic boom propagation (Davy & Blackstock 1971), supersonic combustion systems (Marble et al. 1990, Yang et al. 1994), shock propagation through foams and bubbly liquids (Ball & East 1999, Collins et al. 2005, Delale et al. 2005), the fragmentation of gallstones or kidney stones by shock waves (Delius et al. 1998, Eisenmenger 2001, Gracewski et al. 1993), and high-energy-density systems such as inertial confinement fusion devices (Lindl et al. 1992, Lindl 1995).

The dynamics of the interstellar medium in spiral galaxies is significantly affected by the strong shock waves generated by supernovae explosion, stellar winds, expanding HII regions, and spiral density waves (Klein et al. 1994). It is universally accepted that the generated shock waves significantly alter the morphology of the cloud (a region of higher density) and lead to turbulent exchange of material and energy between interstellar gases of different temperatures and densities. The bright eastern knot of the Puppis A supernova remnant is responsible for distorting a shock front due to a cloud-shock interaction as seen in images from the Chandra X-ray telescope (Hwang et al. 2005). The physics of mass stripping from the cloud, transfer of energy and momentum to the shocked cloud, and the instabilities created by shocks at the cloud boundary have been modeled with laser-driven high-energy-density SBI experiments (Klein et al. 1994, Hansen et al. 2007).

SAIFs are also encountered in shock-mitigation systems based on two-phase flows in which bubbly liquids and aqueous foam barriers are used to redistribute the impulse of the shock waves (Ball & East 1999, Collins et al. 2005, Delale et al. 2005). The dissipation is attributed to interphase heat transfer and small-scale internal processes within the foam. Aqueous foams exhibit high acoustic impedance and low sound speed, so that shock waves and blast waves are subject to refraction and partial transmission at foam/air interfaces and are delayed within the foam (Ball & East 1999).

In inertial confinement fusion experiments, the temperature and density of the thermonuclear fuel contained in a small (≈ 2 mm) spherical capsule are raised to the values necessary for a fusion reaction to occur by imploding the capsule with a convergent spherical shock wave generated by direct or indirect illumination of the capsule by a large number of high-power laser beams. As the shock wave traverses the solid capsule, the shock-induced turbulent mixing (consequent to the shock wave not being perfectly spherical and the capsule surface containing small-amplitude,
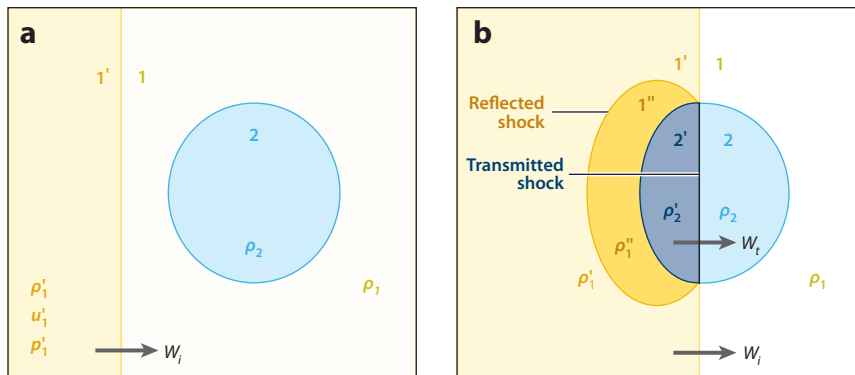
Figure 1

Schematic diagram of shocked interface system in the case of a shock-bubble interaction: (*a*) preshock and
(*b*) postshock.

high-wave-number manufacturing imperfections) leads to the intermingling of the shell material
with the fuel, which can severely degrade the energy yield from the fusion reaction (Lindl et al.
1992, Lindl 1995).

   Although plasma physics plays a fundamental role in the SAIF occurring in astrophysics and
in inertial confinement fusion experiments, this review deals exclusively with the fluid dynamics
of the flows. Both shock-accelerated cylinders and spheres can be categorized under the general
SBI label, with the cylinder and the sphere representing a two-dimensional (2D) and a 3D bubble,
respectively. The organization of this review is as follows. Section 2 provides a general discussion of
the physics of SBIs. Sections 3 and 4 review the experimental work and the analytical and numerical
work appearing in the literature, respectively. Finally, Section 5 provides a brief overview of other
physical scenarios of practical value for which one frequently observes the interaction of a shock
wave with a spherical/cylindrical inhomogeneity.

2. PHYSICS OF THE SHOCK-BUBBLE INTERACTION

The shocked interface system consists of five different regions, as shown in **Figure 1**: Region 1
is unshocked ambient gas, region 2 is unshocked bubble gas, region 1′ is shocked ambient gas,
region 2′ is shocked bubble gas after the passage of the transmitted shock, and region 1″ is shocked
ambient gas after the passage of both the initial shock and the reflected shock or rarefaction wave.
Flow variables are identified using a subscript 1 for the surrounding (ambient) fluid and a subscript
2 for the bubble fluid, and primes are used to denote the number of shock or rarefaction waves
that have passed over the fluid. Hence, p_1 and p_2 represent the preshock pressures of the ambient
and bubble fluids, respectively, and p_1' and p_2' represent the pressures after the passage of first
shock.

2.1. Shock Compression and Acceleration

The passage of a shock over a bubble leads to compression of the bubble and a sudden jump in
fundamental thermodynamic quantities such as pressure, temperature, and density. The bubble
pressure, temperature, and density, as well as its translational velocity, must all increase, according
to the Rankine-Hugoniot conditions, as the transmitted shock wave passes through the bubble.

Considering that the flow across the shock wave is adiabatic (i.e., no heat addition or removal at the boundary), the jump in the fundamental quantities can be derived from the conservation of mass, momentum, and energy equation. In the shock-wave reference frame, the normal shock relations are stated as

$$\rho W = \rho' \left(W - u' \right), \quad (Continuity) \tag{1}$$

$$p + \rho W^2 = p' + \rho' \left(W - u' \right)^2, \quad (Momentum) \tag{2}$$

$$h + \frac{W^2}{2} = h' + \frac{(W - u')^2}{2}, \quad (Energy) \tag{3}$$

where W indicates shock-wave velocity, u' denotes the velocity of the fluid behind the shock wave, and $h(h')$ defines the enthalpy of the fluid ahead of (behind) the shock wave. For a calorically perfect gas with a known specific heat ratio γ, we can add the thermodynamic relations

$$p = \rho R T, \tag{4}$$

$$h = \frac{\gamma R T}{(\gamma - 1)}, \tag{5}$$

where R is the specific gas constant. Equations 1–5 constitute five equations with five unknowns (ρ', u', p', h', and T'). Hence, they can be solved algebraically to obtain the shocked state variables in the case of a normal shock propagation through a planar gaseous interface (Anderson 2003, Liepmann & Roshko 1957).

2.2. Nonlinear-Acoustic Effects

The second aspect of SBI deals with nonlinear-acoustic effects, which refer to the refraction, reflection, and diffraction of the incident shock wave by the bubble. The bubble alters the shape and propagation pattern of the shock wave by nonlinear-acoustic mechanisms associated with the interface curvature and acoustic impedance mismatch at the interface. Owing to the acoustic impedance mismatch at the bubble boundary, the bubble acts like a diverging or converging lens (Dimotakis & Samtaney 2006). The acoustic impedance, $\mathcal{R} = \rho c$, is defined as the product of the density of the gas and the sound speed (c) in that medium. The acoustic impedance is a thermodynamic property and is peculiar to the propagation medium. It is a measure of the stiffness of a material, in the sense that it is a proportionality constant between impressed velocity and applied pressure (the usual elastic moduli, however, correspond to ρc^2) (Thompson 1984). The change in acoustic impedance between two media is known as the impedance mismatch, $\delta \mathcal{R} = \mathcal{R}_2 - \mathcal{R}_1$. Neglecting the curvature of the bubble interface, shock passage over the bubble surface can be analyzed easily using a 1D approach.

Figure 2 shows shock-wave transmission and reflection in a gas slab labeled fluid 2. Two different postshock scenarios are analyzed based on the sign of the impedance-mismatch term ($\delta \mathcal{R}$) at the interface. If $\delta \mathcal{R} > 0$, the shock wave decreases in speed after transmission, and to maintain mechanical equilibrium at the interface, the initial gas must contract. Therefore, in this scenario the reflected wave is a shock wave (**Figure 2b**). Conversely, if $\delta \mathcal{R} < 0$, the shock wave increases in speed after transmission, and to maintain mechanical equilibrium at the interface, the initial gas must expand. Thus, in this scenario the reflected wave is a rarefaction wave (**Figure 2c**). The transmitted wave is always a shock wave independent of the impedance of the medium and shape of the interface. **Figure 3** shows the wave diagram for both cases.
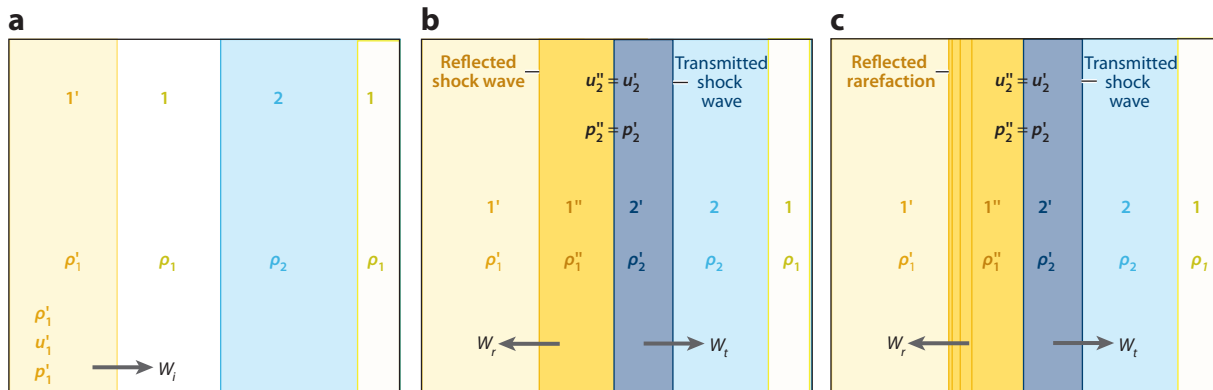
Figure 2

Schematic diagram of 1D shock-wave transmission and reflection in a gas slab: (*a*) preshock; (*b*) postshock, $\mathcal{R}_2 > \mathcal{R}_1$; and (*c*) postshock, $\mathcal{R}_2 < \mathcal{R}_1$.

Shock propagation through the bubble can be considered as an extension of the gas-slab problem. Let us consider the case in which fluid 2 in the gas-slab scenario is replaced by a cylindrical or spherical bubble. **Figure 4** highlights the effect of the bubble interface curvature, on the shock refraction pattern for two different impedance-mismatch scenarios. **Figure 4a** shows the shock refraction pattern for $\delta\mathcal{R} > 0$. This situation is commonly referred to as convergent geometry. The transmitted shock wave is concave in shape and runs behind the unrefracted incident shock, and the reflected wave is a shock. **Figure 4b** highlights the shock refraction pattern for the divergent geometry in which $\delta\mathcal{R} < 0$ at the interface, and the reflected wave is a rarefaction. In this situation, at low angles of incidence, regular refraction occurs where the transmitted wave and incident wave intersect the interface at the same point. At higher angles, various aspects of irregular refraction are observed (Henderson 1989, Henderson et al. 1991). A transmitted shock wave quickly transits the bubble, and a Mach stem, precursor shock, and triple point form just outside the interface. Such features are absent in the case of the convergent geometry. In this case for high density contrast (density ratio larger than 1.5), irregular refraction of the shock wave leads to shock focusing. As depicted in **Figure 5**, a portion of the shock-wave front sweeping around the bubble periphery is diffracted, meaning that it is turned toward the axis so that the surface of discontinuity remains nearly normal to the interface (Haas & Sturtevant 1987, Niederhaus et al. 2008).
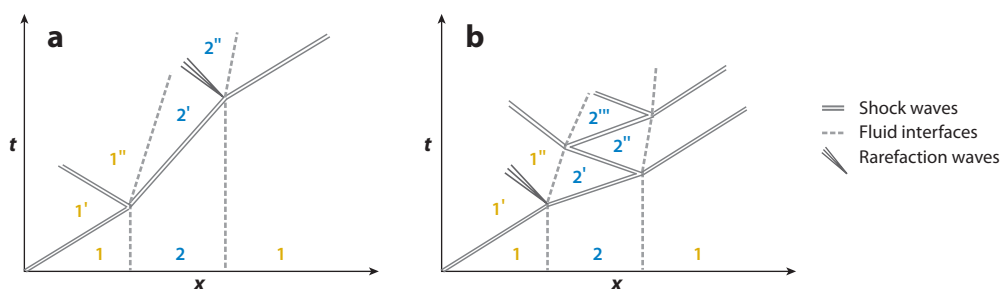

Figure 3

Wave diagram of 1D shock transmission and reflection in a gas slab: (*a*) $\mathcal{R}_2 > \mathcal{R}_1$ and (*b*) $\mathcal{R}_2 < \mathcal{R}_1$. Solid double lines indicate shock waves, dashed lines indicate fluid interfaces, and triple diverging solid lines indicate rarefaction waves (Niederhaus 2007).
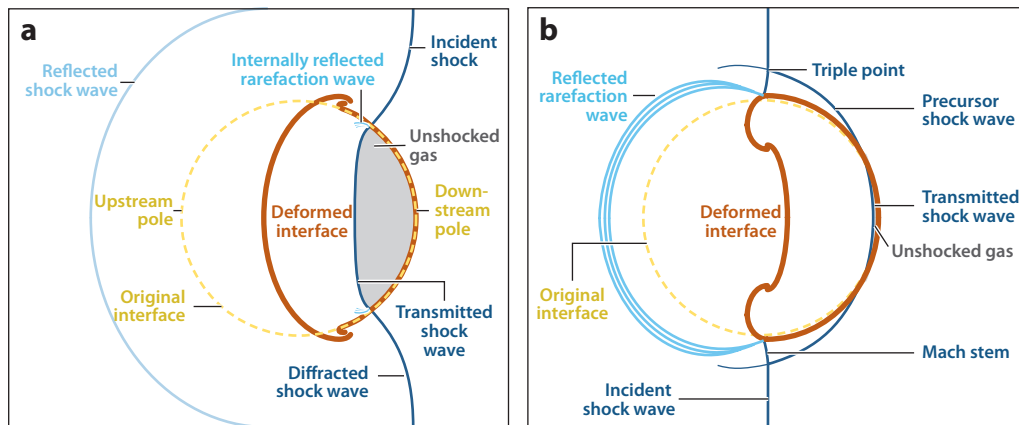
Figure 4

Schematic representation of shock-bubble interaction flow field and shock refraction patterns in a (*a*) convergent ($\delta\mathcal{R} > 0$) scenario and (*b*) divergent ($\delta\mathcal{R} < 0$) scenario, shortly after initial shock-wave transit. Incident shock-wave propagation is left to right (Niederhaus 2007).

The diffracted shock waves then meet at the downstream pole. **Figure 5** shows the different stages of shock refraction in the case of convergent geometry, leading to the shock focusing at the downstream pole of the bubble. The diffracted shock waves' collision, along with the focusing of the transmitted shock wave, produces an intense pressure jump and initiates additional baroclinic vorticity deposition. Secondary shock waves are generated due to shock focusing, which can lead to dramatic changes in the observed flow field at late times. This effect can be compared to a reshock phenomenon, familiar from Richtmyer-Meshkov flows in shock tubes.

Richtmyer-Meshkov flows: shock-driven interfacial instability

2.3. Vorticity Production and Transport

The third, and probably most important, aspect of SBIs is the vorticity deposition due to the misalignment of the pressure and the density gradients. As this field of shock waves (including the primary incident shock wave, along with the secondary refracted, reflected, diffracted, and focused waves) passes over the bubble, vorticity is produced in the flow. Vorticity is defined as the curl of the velocity

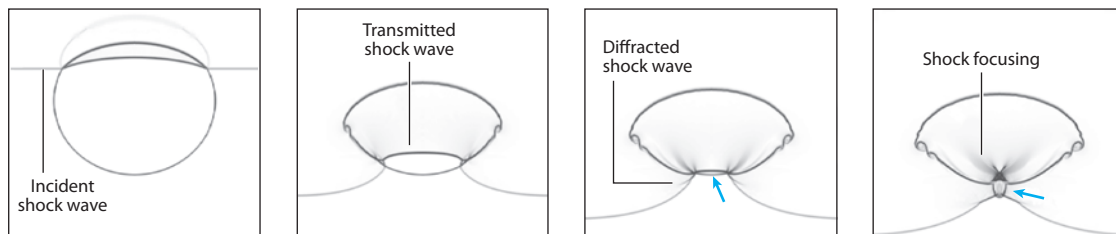$$\boldsymbol{\omega} \equiv \nabla \times \mathbf{U}. \tag{6}$$

Figure 5

Representative, schematic view of shock focusing in the case of convergent geometry. The arrow in the diagram indicates the location of the shock focusing. Incident shock-wave propagation is top to bottom.

Taking the curl of the momentum equation for a compressible flow, one obtains the vorticity transport equation, given as

$$\frac{D\boldsymbol{\omega}}{Dt} = (\boldsymbol{\omega} \cdot \nabla)\mathbf{U} - \boldsymbol{\omega}(\nabla \cdot \mathbf{U}) + \frac{1}{\rho^2}(\nabla\rho \times \nabla p) + \nu\nabla^2\boldsymbol{\omega}. \tag{7}$$

The first term on the right-hand side, $(\boldsymbol{\omega} \cdot \nabla)\mathbf{U}$, is the vortex-stretching term, which is essential for the discussion of 3D turbulence and mixing. This term represents the stretching, as well as the turning and tilting, of the vortex lines by gradients in the velocity field. Vortex stretching also reflects the principle of conservation of angular momentum. Stretching decreases the moment of inertia of fluid elements that compose a vortex line, resulting in an increase of their angular speed. The vortex-stretching and -tilting term is absent in 2D flows, in which $\boldsymbol{\omega}$ is perpendicular to the flow.

The second term on the right-hand side, $\boldsymbol{\omega}(\nabla \cdot \mathbf{U})$, represents the vortex dilatation term, which is important only in the case of highly compressible fluids. The last term on the right-hand side, $\nu\nabla^2\boldsymbol{\omega}$, represents the rate of change of $\boldsymbol{\omega}$ due to molecular diffusion of vorticity, in the same way that $\nu\nabla^2\mathbf{U}$ represents the acceleration due to the diffusion of velocity. Dissipative effects can be neglected generally because of the low physical viscosities of the fluids considered ($\mu \sim 10^{-5}$ Pa $\cdot$ s) and the short timescales ($t \sim 10^{-3}$ s) over which the flow evolution is studied. The third term on the right-hand side, $(\nabla\rho \times \nabla p)/\rho^2$, is the baroclinic term, which represents the rate of vorticity generation due to baroclinicity in the flow. It shows that the misalignment of the local pressure and density gradients leads to the generation of vorticity in the flow field.

In the case of an SBI, initially $\boldsymbol{\omega} = 0$ everywhere. Therefore, the vortex-stretching and -dilatation term in Equation 7 drops out. In the absence of dissipative effects, Equation 7 reduces to

$$\frac{D\boldsymbol{\omega}}{Dt} = \frac{1}{\rho^2}(\nabla\rho \times \nabla p), \tag{8}$$

suggesting that baroclinicity is the only source for vorticity production in the flow field at time zero. The vorticity distribution at the early stage of the SBI is shown in **Figure 6**.

Vorticity is deposited locally on the fluid interface during shock-wave propagation across the bubble. The magnitude of the vorticity deposited locally is determined by the noncollinearity of $\nabla\rho$ and ∇p. The maximum misalignment is at the diametral plane, and the maximum vorticity is deposited at this location. This leads to the formation of a pair of straight parallel vortex lines or a vortex ring near the diametral plane, depending on whether the inhomogeneity is 2D (cylindrical) or 3D (spherical). The rotation of these vortices is determined by the orientation of the density gradient at the bubble interface. **Figure 6** shows the direction of rotation in the case of convergent and divergent geometry of the bubble. It is evident that these vortices are the dominant feature of the flow.

The vorticity-generation mechanism is similar to that found in the Richtmyer-Meshkov instability. Although the shock refraction pattern is dictated by the impedance mismatch at the interface, this phenomenon only exists during the early phase of the flow. After several shock-passage times (D/W), the features observed in the flow field are dominated by the vortical motion. Henceforth, we use the Atwood number defined as $A = (\rho_2 - \rho_1)/(\rho_2 + \rho_1)$ in this review to indicate the effect of density contrast at the bubble interface rather than the impedance mismatch. For the gas pairs considered here, $A > 0$ refers to convergent geometry ($\delta\mathcal{R} > 0$), and $A < 0$ refers to divergent geometry ($\delta\mathcal{R} < 0$). It is well-known (Thompson 1984) that in some unusual conditions it is possible to have convergent refraction ($\delta\mathcal{R} > 0$), even if $A < 0$, and vice versa. This is possible if the effect from the specific heat ratios offsets the changes in density, and such cases do not appear in this review.

Vortex stretching: represents the stretching, as well as the turning, of the vortex lines by gradients in the vortex fields

Baroclinicity: misalignment of the local pressure and density gradients
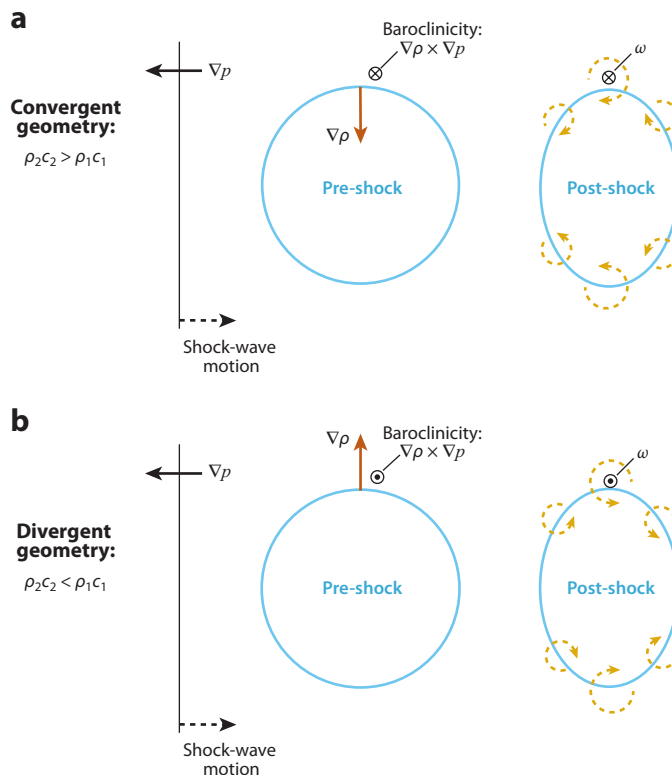
Figure 6

Representative, schematic view of the arrangement of vectors in baroclinic vorticity deposition during and after initial shock transit in shock-bubble interactions in (*a*) convergent and (*b*) divergent geometry.

The three underlying physical processes outlined above are nonlinearly coupled together. Their simultaneous action in an SBI leads to the development, in many cases, of highly complex regions of strong, disordered rotational motion and mixing.

3. EXPERIMENTAL WORK

3.1. Conventional Shock-Tube Studies

Experimental investigations of the interaction of shock waves with curved interfaces have been inspired by the pioneering works performed by Markstein (1957a,b) and Rudinger (1958), who studied the interaction of a shock wave with a flame front having a nearly spherical shape. The primary focus of the study was to quantify the effect of the shock on the volumetric rate of burning. The interaction of pressure waves with density gradients is a fundamental source of long-lived vorticity in fluids and is particularly important in combustion, as the release of the chemical energy produces both pressure and density disturbances in the fluid. These disturbances then interact, producing significant vorticity in the flow field. In his classic experiment, Markstein (1957b) showed how combustion enhancement followed the acceleration of an initially curved flame surface by a shock wave. Curved flame fronts, when accelerated by a shock wave, undergo heavy distortions such as inflection and spike formation. The volumetric rate of burning is amplified after the shock
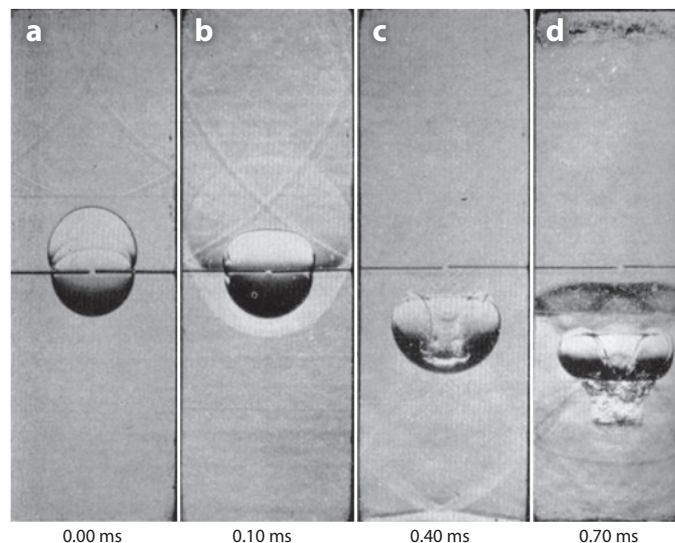
Figure 7

Interaction of a shock wave and a flame of initially roughly spherical shape. The pressure ratio of incident shock wave is 1.3; the stoichiometric butane-air mixture ignited at the center of the combustion chamber 8.70 ms before the origin of the timescale (Rudinger 1958). The time relative to the initial shock-wave impact is (*a*) 0.00 ms, (*b*) 0.10 ms, (*c*) 0.40 ms, and (*d*) 0.70 ms.

interacts with the flame. Markstein also studied the interaction of a shock wave with a nearly spherical flame, and **Figure 7** shows schlieren images from one of Markstein's experiments. A weak shock passes through a roughly spherical flame approximately 15 cm from the bottom of the combustion chamber, which contains a stoichiometric mixture of *n*-butane and air. In **Figure 7*a***, the shock wave appears to be less than 1 cm from the flame boundary (the flame actually appears more oblong than spherical). In **Figure 7*b***, one can clearly see the compression of the flame front and an upward-moving curved rarefaction wave. The central spike of unburned gases traverses the lower portion of the flame front (see **Figure 7*c***), leading to the formation of a vortex ring. This enhanced flow, due to the vortex ring, leads to the formation of a very-fine-grained turbulent burning zone.

To analyze the fluid dynamic aspects of vorticity generation, one may more easily study the problem in a nonreactive medium. If the flame is not a continuous surface but contains discrete pockets of burned or unburned gas surrounded by gases of different density, such as may exist around evaporating fuel droplets, another mechanism to increase the volumetric burning rate may come into play. Rudinger & Somers (1960) considered the response of such isolated regions of different density to impulsive acceleration without the complications of the combustion process. They looked at the more fundamental problem of the interaction of a planar shock wave with light- or heavy-gas spherical or cylindrical inhomogeneities, produced using either a spark discharge or small jets of H_2, He, or SF_6. After acceleration by a shock wave, the small regions in a flow in which the density was different than that of the surrounding gas moved faster or slower than the latter, depending on whether their density was lower or higher than that of the main flow. Rudinger & Somers verified that these effects resulted from vortical instabilities excited during shock-wave passage over the spark column, and they introduced a simple model for the relative velocity of the shocked bubble. The interaction of a shock wave with a cylindrical or spherical gas inhomogeneity has become more commonly known as the SBI. Inspired by their

seminal work, the last two decades have provided a rich database of literature for the study of the SBI.

Haas & Sturtevant (1987) reported on experiments conducted in a horizontal shock tube studying the interaction of a light- or heavy-gas bubble subjected to a planar shock wave. The spherical shapes were produced using soap bubbles filled with either a light or a heavy gas, whereas the cylindrical inhomogeneities were encapsulated in thin nitrocellulose membranes. The wave-front geometry and the deformation of the gas volume were visualized by shadowgraph photography. Wave configurations predicted by geometrical acoustics, including the effects of refraction, reflection, and diffraction, were compared with the observed flow field. It was shown that, in the case of a cylindrical or spherical volume filled with a heavy (low-sound-speed) gas, the wave that passes through the interior focuses just on the downstream pole of the cylinder. Alternatively, a wave passing through a light (high-sound-speed) gas strongly diverges. The distortion of the helium cylinder in an air environment at late times showed that the interaction of a shock wave with a gas lighter than its surrounding develops into a pair of vortices that move faster than the ambient fluid. In the case of a helium sphere at late times, it was observed that the primary vortex ring splits off from the main structure and propagates along the axis of symmetry.

In the early 1990s, Jacobs (1992, 1993) implemented a new technique in a horizontal shock tube, in which a laminar jet was used to produce the gas cylinder, eliminating the need for a membrane to encapsulate the heavy or light gas (Haas & Sturtevant 1987). The shortcomings of shadowgraphy were eliminated by utilizing planar laser-induced fluorescence (PLIF). The test gas (sulfur hexafluoride or helium) was seeded with a small amount of biacetyl; the jet of test gas was accelerated by a planar shock wave traveling in a direction perpendicular to the jet axis; and a cross section of the flow was illuminated with a laser sheet that caused the biacetyl to fluoresce. These improvements not only resulted in a higher quality of flow visualization (see **Figure 8**), but also allowed for the measurement of species concentration, and hence the mixing that is produced by the shock/cylinder interaction.

Tomkins et al. (2003) reported on the evolution and interaction of two shock-accelerated SF_6 cylinders as an extension to the single-cylinder configuration. Planar Mie scattering was utilized for flow visualization. An intensified CCD (charge-coupled device) camera, aligned normal to the laser sheet, was used to capture the light scattered from the bubble gas (seeded with a small amount of glycol/water fog droplets), and velocity measurements were performed using digital particle image velocimetry. The visualization revealed that the flow morphology is highly sensitive to the initial separation between the cylinders. Later, the two-cylinder system was extended to a three-or-more cylinder configuration by Kumar et al. (2005), with one of five different configurations of SF_6 cylinders, surrounded by air, being impulsively accelerated to produce one or more pairs of interacting vortex columns. The flow was visualized using PLIF in the plane normal to the axes of the cylinders, and it was found that the number, configuration, and orientation of gaseous cylinders affect the shock-induced mixing in terms of the generation of interfacial area. The purpose of this study was to understand fluid mixing in SAIFs from the more fundamental point of view of stretching of material lines at early times (approximately the first 220 μs after shock impact). Such flows are characterized by a Schmidt number of approximately 1 and a Reynolds number of approximately 25,000 (based on circulation and mean kinematic viscosity), and hence such studies are possible at early times only. Yang et al. (1993) introduced a specific stretching rate exponent, λ, defined as

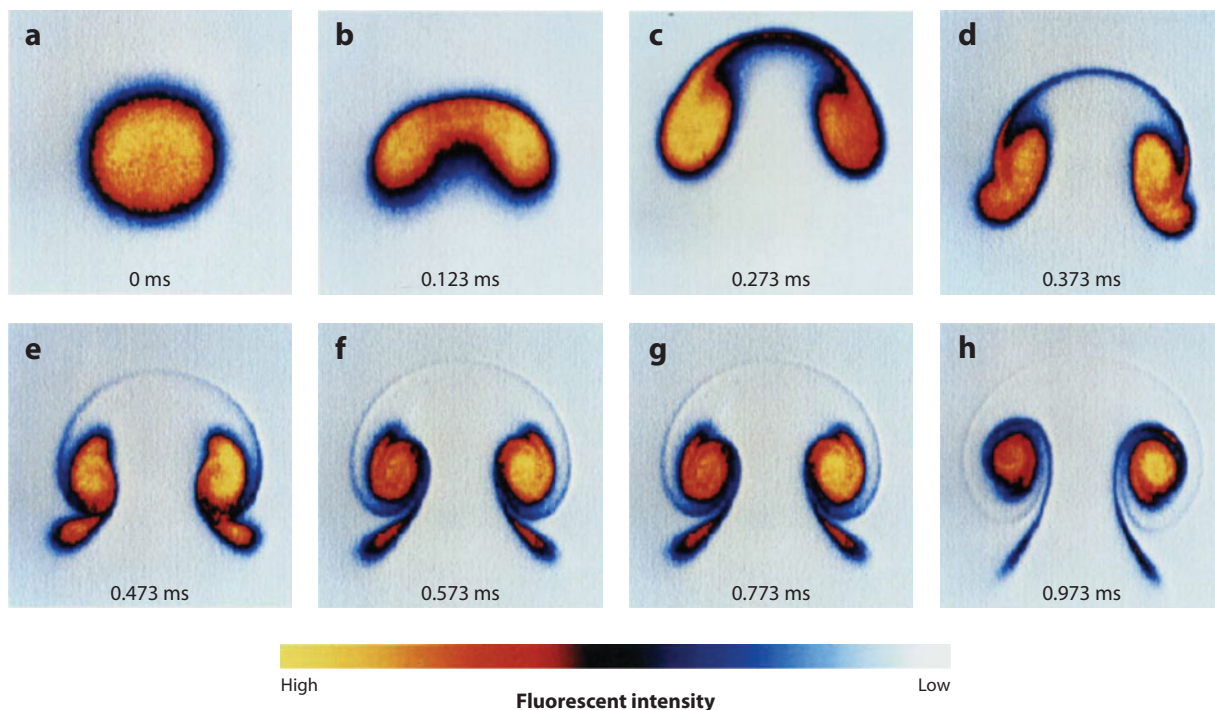$$\frac{L(t)}{L(t=0)} = A \exp\left(\frac{\lambda t}{t_0}\right), \tag{9}$$

Figure 8

Flow-field evolution from an $M = 1.093$ shock-wave interaction with a cylindrical helium inhomogeneity (Jacobs 1992). The planar laser-induced fluorescence images give a cross-sectional view of the evolving structure: (*a*) the initial jet, (*b*) $t = 0.123$ ms after the passage of the shock wave, (*c*) $t = 0.273$ ms, (*d*) $t = 0.373$ ms, (*e*) $t = 0.473$ ms, (*f*) $t = 0.573$ ms, (*g*) $t = 0.773$ ms, (*h*) and $t = 0.973$ ms.

where $L(t)$ is the length of a marked material line at time t, $L(t = 0)$ is the interface length at time $t = 0$ (time at which the shock first interacts with the gaseous cylinder configuration), A is a constant, and $t_0 = D/2c_1$ (i.e., the time required for sound to travel the radius of the nozzle) is used to normalize time. They also measured the integral mixing widths for these five configurations and found that the integral widths collapse at early times and are thus not a good measure of the effect of the initial condition on flow mixing; however, the specific stretching rate exponent, λ, measured by the authors appears to be a good measure and clearly distinguishes the various configurations studied.

Kumar et al. (2007) again studied, both experimentally and numerically, the interaction of Mach-1.2 shock wave with three gaseous SF_6 cylinders separated in the spanwise direction at a spacing ratio of 1.5. The focus of their work was to understand the sensitivity of the resulting flow morphologies to rather small perturbations (changes in the structure on the diffused material between the gaseous cylinders) in the initial conditions using PLIF flow visualization. Four distinct postshock morphologies were obtained due to such perturbations in the nominally identical initial conditions, i.e., produced by the same nozzle. This was in contrast to the two-cylinder configuration studied by Tomkins et al. (2003). This study showed that the complexity of the system considerably increases as the number of gaseous cylinders in the spanwise direction is increased, due to increased vortical interactions. The gas curtain (Budzinski et al. 1994, 1996; Jacobs et al. 1993; Prestridge et al. 2001), which is also a canonical problem being studied to
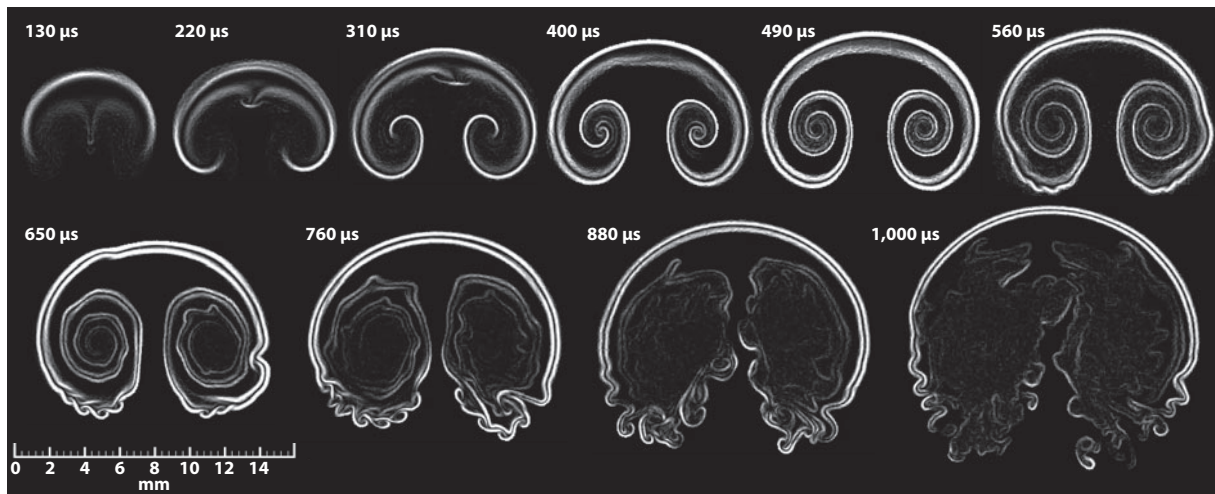
Figure 9

Spatial maps of the mixing rate (scalar dissipation rate) of a heavy gas, $\chi/c_{\max}^2$, with time t (Tomkins et al. 2008).

understand Richtmyer-Meshkov instability induced mixing, can be considered as a problem with several, closely spaced, gaseous cylinders in the spanwise direction.

Tomkins et al. (2008) revisited the problem of fluid mixing resulting from the interaction of a Mach-1.2 shock wave with a single gaseous cylinder using quantitative PLIF. Experimental measurements of the spatial distribution of instantaneous scalar dissipation rates, $\chi(\mathbf{x}, t) \equiv \mathcal{D}(\nabla c \cdot \nabla c)$, were obtained, for the first time, at several times after shock impact (see **Figure 9**). Here $\mathcal{D}$ is the molecular diffusivity between the gases. These measurements revealed detailed mixing mechanisms that are not provided by conventional integral mixing width measurements. The authors observed three regions of mixing in such a flow: the bridge connecting the two primary vortices, the vortex cores, and the Kelvin-Helmholtz (KH) region. In the first region, mixing is associated with gradient intensification due to the straining velocity field. This bridge region, which appears as a relatively smooth (nonturbulent) stretch of material connecting two primary vortices in the visualization images, surprisingly contributes 40% to the mixing up to ~1,000 μs after shock impact. Studies of the distribution of χ showed that the bridge (or primary instability) plays a dominant role in contributing the highest values of χ, the most intense mixing in the flow. In the KH regions (regions on the outer surfaces where KH rollers are visible) and the vortex cores (regions toward the center of the core where secondary instabilities and spiral roll up occur), the mixing is also driven by large-scale strain fields at early times, although the induced motions due to vorticity create both gradient intensification and an increase in surface area due to developing spirals. At intermediate times, the KH instability appears along outer regions of the flow, and a mix of Rayleigh-Taylor and KH instabilities appears in the cores. At much later times, the mixing is primarily associated with stretching and folding of the concentration fields due to motions induced by the secondary instabilities.

Recently, a number of experiments have been reported on the interaction of a planar shock wave with a spherical gas inhomogeneity (soap bubble), beginning with the work of Layes et al. (2003, 2005, 2009). They were the first to use high-speed shadowgraph imaging to capture the interaction of shock waves at $M \leq 1.25$ in air with spherical soap bubbles filled with krypton, nitrogen, or helium. Layes et al. produced further qualitative characterization of the flow evolution

KH: Kelvin-Helmholtz

**Rayleigh-Taylor flows:** gravitational force–driven interfacial instability

for SBIs and showed that for each case they studied, at late times, the streamwise dimension of the bubble grew at a constant rate and the shocked bubble moved at a constant translational speed. More extensive analysis of the experimental results, as well as data for $M \leq 1.68$, can be found in the dissertation of Layes (2005), and in the work of Giordano & Burtschell (2006) and Layes & LeMétayer (2007).

Experimental results have appeared recently in the work of Ranjan et al. (2005) for SBIs at higher Mach numbers than those studied by Haas & Sturtevant (1987) or Layes et al. (2003, 2005). Ranjan et al. studied the case of a soap bubble filled with argon, accelerated by an $M = 2.88$ shock wave in nitrogen, using planar laser diagnostics to capture the flow-field development in a section near the bubble midplane. Furthermore, Ranjan et al. (2007, 2008a) used similar diagnostic techniques to study the case of a helium-filled bubble, accelerated by an $M = 2.95$ shock wave. In both cases, the shocked bubble reached a constant translational velocity at late times, as reported by Layes et al. (2003, 2005), but distinct secondary vortex rings formed at later times as well, which had not been observed previously in experimental results for lower Mach numbers. These long-lived secondary vortex rings can be seen clearly in the planar-laser-illuminated experimental images and their counterpart shown in **Figure 10**. The emergence of these secondary vortices is significant for two reasons. First, they contribute to the elongation of the mixing region, as the two counter-rotating vortex rings tend to pull away from each other and eventually pinch off. Second, vortex rings are stable coherent structures that persist to very late times and propagate downstream at nearly constant velocity. Thus, in SAIFs in which strong irregular shock refraction takes place in the inhomogeneities, long-lived vortex projectiles of this sort may be expected to arise in the flow as artifacts of shock refraction and persist to very late postshock times. More extensive analysis of the experimental results can be found in the doctoral dissertation of Ranjan (2007).

3.2. Laser-Driven Experiments

Several shock-driven experiments for a spherical inhomogeneity have been carried out at high Mach numbers ($M \sim 10$) using both the Omega laser at the Laboratory of Laser Energetics (Robey et al. 2002, Hansen et al. 2007) and the NOVA laser at the Lawrence Livermore National Laboratory (Klein et al. 2000, 2003). Klein et al. (2000) utilized the NOVA laser to generate a strong shock wave ($M = 10$) that traveled within a miniature beryllium shock tube, 750 μm in diameter, filled with a low-density plastic. Embedded in the plastic was a copper sphere 100 μm in diameter. Its morphology and evolution, as well as the shock trajectory, were diagnosed via side-on radiography. Beryllium was used for the shock-tube wall material as it is essentially transparent to the X-rays used to diagnose the target evolution. The experiments showed the initial distortion of the copper sphere into a vortex-ring structure. Klein et al. (2003) compared their previous experimental results (Klein et al. 2000) to detailed 2D and 3D radiation hydrodynamic simulations that showed the initial distortion of the bubble into a vortex ring and later the breakup of the vortex ring due to the azimuthal bending-mode instability (Widnall et al. 1974).

Robey et al. (2002) conducted a similar set of experiments on the Omega laser. They simultaneously performed side-on and face-on radiography to reconstruct the 3D topology of the interaction. This enabled them to visualize both the initial distortion of the copper sphere into a double-vortex-ring structure and the onset of the azimuthal instability. The paper also included a detailed numerical study of the described experiments using a 3D Eulerian adaptive mesh refinement code, which is also the same code later used by Niederhaus (2007) to perform a parametric study for the shock-bubble problem. The numerical study showed that 2D codes are completely inadequate in resolving the observed azimuthal mode structures. The numerical study showed a
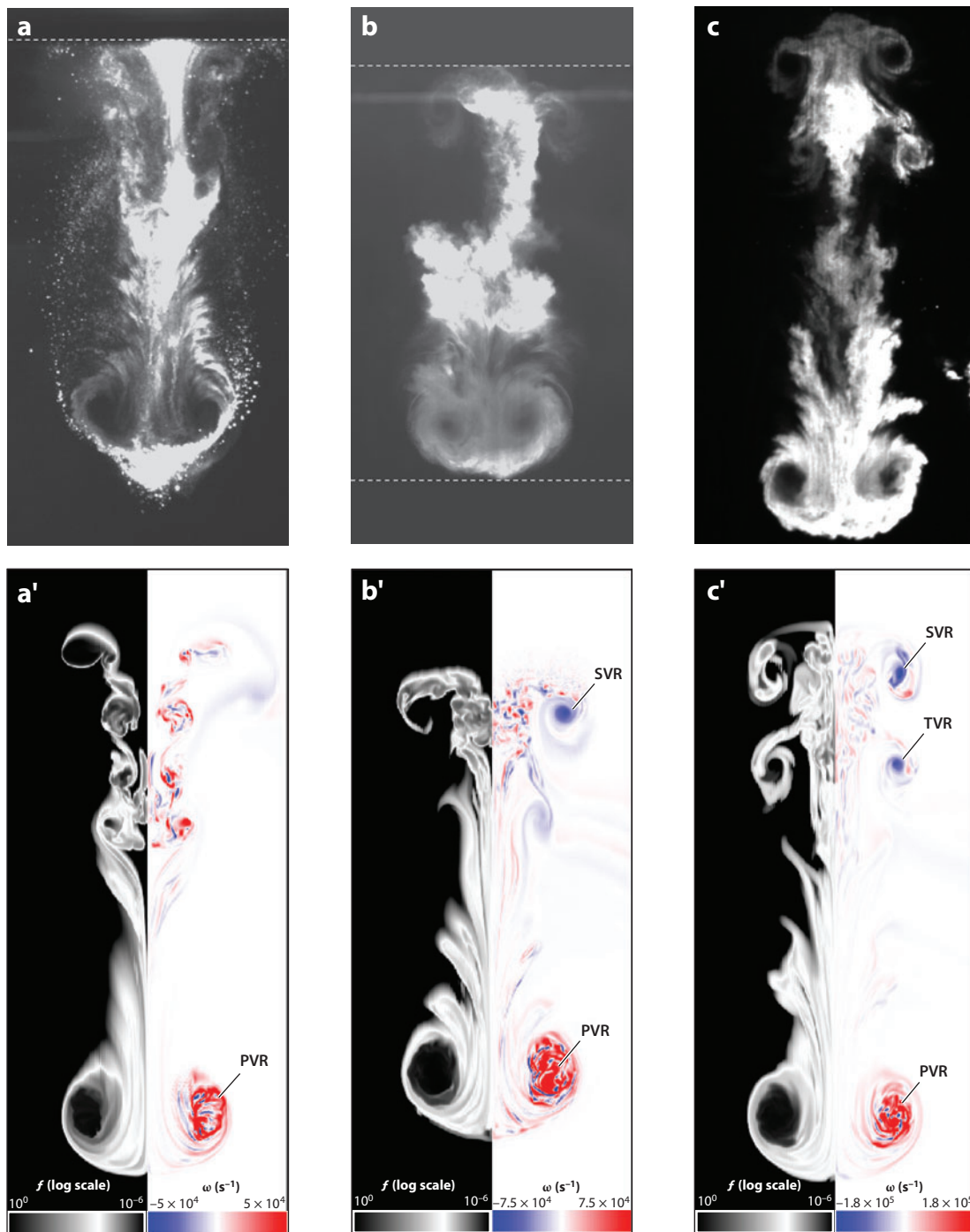
good agreement with the observed distortion of the copper sphere. The breakup of the vortex ring due to the onset of bending-mode instabilities was also captured in the simulations.

Hansen et al. (2007) took the Omega experiments a step further by replacing the area-radiography technique used by Robey et al. (2002) with a point-projection radiography technique, and this vastly increased the number of photons that illuminated the shock tube, resulting in a better signal-to-noise ratio. The images obtained with this technique allowed them to estimate the cloud mass as a function of time. In these experiments they also replaced the copper sphere used previously by other experimenters with an aluminum sphere to study the faster hydrodynamic evolution for the lighter material, so distortion could be studied for a longer time. Hansen et al. showed that the cloud mass as a function of time follows a model of turbulent-mass stripping, strongly suggesting that turbulence plays an important role in the development at late times. These 3D structure development and mass-stripping effects are clearly visible in the X-ray radiographs shown in their figure 3 (Hansen et al. 2007). The authors also showed that the cloud distortion compared quite well quantitatively with the shock-tube experiments reported by Ranjan et al. (2005) for the scaled lengthwise growth of the bubble.

4. ANALYTICAL AND NUMERICAL MODELING

Many different types of models appear in the literature for quantities that may be computed from simulations or measured in experiments. Klein et al. (1994), in particular, have generated simple models for a variety of features of the flow field; however, typical experimental diagnostics do not provide access to many of these features, which include the velocity dispersion and the mean pressure in the bubble. Here, our focus is primarily on quantities that are directly or indirectly measurable in shock-tube experiments. These include models for the translational vortex velocity and for the circulation.

Rudinger & Somers (1960) developed a simplified theoretical model for the interaction of a shock wave with a bubble that leads to the calculation of the initial bubble velocity V_b and final vortex velocity V_v. The model assumes that the bubble is initially accelerated by the shock to a velocity V_b, different from the shocked ambient gas velocity u'_1. For the early phase, they treated the bubble as if it were a solid particle. The calculation assumes an impulsive, essentially incompressible acceleration. The impulse per unit volume I transmitted by the shock to the gas bubble is precisely that which the ambient gas would have experienced,

$$I = \rho'_1 u'_1 = \rho'_2 V_b + k\rho'_1 \left(V_b - u'_1 \right), \qquad (10)$$

where ρ'_2 is the postshock bubble gas density and ρ'_1 denotes the postshock ambient gas density. The term $\rho'_1 k(V_b - u'_1)$ represents the impulse transmitted to the ambient gas around the bubble due to the bubble motion, and k is the inertial coefficient or apparent additional mass fraction. For a spherical bubble, $k = 0.5$, and for an infinitely long cylinder moving at right angles to its axis, $k = 1.0$ (Lamb 1945). From Equation 10, the bubble velocity immediately after the passage

←——

Figure 10

Late-time flow-field visualizations of an He bubble in air or N_2. The top row contains experimental images, and the bottom row numerical ones. Numerical images show (*on the left*) the helium volume fraction f on a logarithmic gray scale peaked at $f = 10^{-4}$ and (*on the right*) vorticity magnitude ω. Dimensionless times τ are (*a*) 105.8, (*a'*) 105.8, (*b*) 63.4, (*b'*) 63.5, (*c*) 69.5, and (*c'*) 63.5. The characteristic times and Mach numbers (for a bubble of initial diameter 3.81 cm) are (*a,a'*) $t' \approx 15.3$ μs, $M = 1.45$; (*b,b'*) $t' \approx 12.3$ μs, $M = 2.08$; and (*c,c'*) $t' \approx 9.7$ μs, $M = 2.95$. Note that $\tau = tW_t/R$ here. PVR, primary vortex ring; SVR, secondary vortex ring; TVR, tertiary vortex ring.

of the shock wave is given by

$$V_b = \left(\frac{1+k}{\sigma + k} \right) u_1', \tag{11}$$

where $\sigma = \rho_2'/\rho_1'$ is the postshock density ratio. The second step of the analysis deals with the transformation of the gas bubble into a vortex, where the energy absorbed by the vortex is provided by the kinetic energy of the initial motion, which leads to the decrease of the relative velocity

$$V_v - u_1' = \beta \left(V_b - u_1' \right). \tag{12}$$

Using a calculation by Taylor (1953) for the generation of a vortex ring by the impulsive acceleration of a disk, they arrive at the vortex velocity,

$$V_v = \left(1 + \beta \frac{1 - \sigma}{\sigma + k} \right) u_1', \tag{13}$$

where $\beta = 0.436$ (Taylor 1953) for the vortex ring (spherical bubble scenario) and $\beta = 0.203$ (Rudinger & Somers 1960) for the infinitely long vortex pair (cylindrical bubble scenario). The Rudinger-Somers vortex-ring velocity model is simple and useful; for fixed σ, it yields a normalized velocity V_v/u_1' that is invariant in M. Because of the uncertainty in the effective shape of the bubbles in the experiments, Rudinger & Somers found that the measured vortex velocities fell between those predicted using Equation 13 with the value of β corresponding to spheres and cylinders.

The first detailed numerical investigation of the SBI in two dimensions was performed by Picone & Boris (1988), who modeled the experiments conducted by Haas & Sturtevant (1987) for both cylinders and spheres. Although their 2D simulations only achieved a grid resolution of fewer than 50 cells per bubble radius (R_{50}), they captured the development of the vortical features observed by Haas & Sturtevant. They also presented a model for the calculation of the late-time bubble velocity and the magnitude of the vortex strength, or circulation, Γ. Picone & Boris used this approximation to set the parameters for adaptive gridding in Eulerian simulations for SBIs but did not comment on the effectiveness of the model in comparison with experimental or numerical results. Although intended to capture the motion of the entire shocked bubble, the approximation is useful as a model of the motion of the vortex itself. The circulation Γ is a scalar quantity having considerable importance in the description of the vortical flows. The circulation Γ is defined around a simple closed curve C as a line integral of the velocity given as

$$\Gamma = \oint_C \mathbf{U} \cdot ds. \tag{14}$$

It follows from Stokes's theorem that the circulation around a reducible curve is equal to the flux of vorticity through an open surface A bounded by the curve; that is,

$$\Gamma = \int_A \boldsymbol{\omega} \cdot d\mathbf{S}. \tag{15}$$

The circulation model provided by Picone & Boris is based on the initial properties of the shocked gas, unshocked ambient gas, and the bubble. They utilized Equation 15 to obtain the circulation in one half of the bubble, with the only source term for the vorticity being the baroclinic term. Picone & Boris's circulation model may be written as

$$\Gamma_{PB} \approx 2u_1' \left(1 - \frac{u_1'}{2W_i} \right) \left(\frac{D}{2} \right) \ln \left(\frac{\rho_1}{\rho_2} \right), \tag{16}$$

and the vortex velocity by

$$V_v \approx u_1' + \frac{\Gamma_{PB}}{2\pi D_v}, \tag{17}$$

where D_v is the major diameter of the vortex ring, and D is the initial diameter of the bubble.

Yang et al. (1994) investigated the shock-cylinder interaction numerically and worked along the same path as Picone & Boris to calculate the circulation. The circulation predicted by Yang et al.'s model (the YKZ model) is

$$\Gamma_{\text{YKZ}} \approx \frac{2D}{W_i} \frac{p_1' - p_1}{\rho_1'} \left(\frac{\rho_2 - \rho_1}{\rho_2 + \rho_1} \right). \tag{18}$$

Yang et al. presented results from 2D simulations for the interaction of a shock wave with a cylindrical bubble of helium in an air environment, at Mach numbers $M = 1.05 \leq M \leq 2.0$ (several scenarios with larger density ratios $\chi < 1$ were also simulated). [We use χ to denote the density ratio for the rest of the review, although we use it in previous sections above to denote the scalar mixing rate. This has been done to keep the review aligned with the terminology widely accepted in the community.] The simulations used an Eulerian flux-corrected-transport method and a spatial resolution of R_{20}. The results showed that the model predicted the circulation obtained from simulations to within approximately 15% error, whereas Picone & Boris's model was again found to overestimate the circulation consistently.

Quirk & Karni (1996) reported a detailed numerical study of the SBI utilizing a sophisticated adaptive mesh refined algorithm, with a nonconservative shock-capturing scheme. The adaptive mesh refinement technique enabled them to produce high-resolution results at low cost, and the simulations successfully resolved the shock refraction pattern and vortical features observed by Haas & Sturtevant. Several additional numerical studies have been carried, which were also motivated by the experimental work of Haas & Sturtevant. Winkler et al. (1987) simulated the interaction of an $M = 2$ shock wave with a spherical bubble of a relatively dense gas to highlight the observed development of a supersonic vortex ring downstream from the bubble in the postshock flow. Cowperthwaite (1989) produced 2D simulations of the distortion and motion of an initially spherical mass of Freon 12 gas suspended in a lighter gas (air or helium) surrounding it. The simulations were carried out to late times, and the velocity of the center of mass of the bubble was calculated as a function of time. A simple model, based on the concepts of drag, added mass, and entrainment, was shown to give a good agreement with the bubble velocity observed in the simulation.

Samtaney & Zabusky (1994) produced an in-depth analysis of the baroclinic vorticity deposition on a planar interface using shock polar analysis. This was extended to the spherical case using a near-normality condition, which in our notation is written as

$$\Gamma_{\text{SZ}} = \left(1 + \frac{\pi}{2} \right) \left(\frac{2}{1+\gamma} \right) (1 - \chi) \left(1 + M^{-1} + 2M^{-2} \right) (M - 1)(D/2)c_1, \tag{19}$$

where χ defines the density ratio across the interface. The model shows that for large χ, circulation is independent of the density ratio, and, for high Mach number flows, circulation has a linear behavior in M. This model has been shown to be effective for the convergent-geometry SBI. Zabusky & Zeng (1998) reported on numerical investigations of the interaction of planar shocks with a Freon 12 axisymmetric spherical bubble in air. In this paper, they extended the early axisymmetric simulations by Picone & Boris (1988) to high Mach numbers up to $M = 5$ and observed the formation of a secondary vortex ring at the apex of the bubble for shock strengths $M = 2.5$ and 5.0. The formation of the secondary vortex ring was attributed to secondary shocks that can arise in the higher-shock-strength scenario. Levy et al. (2003) used an interface-tracking 2D ALE hydrodynamic code to simulate the SBI and were motivated by the experimental work performed by their group. They extended Samtaney & Zabusky's circulation model to the scaling

of the velocity field and showed that the velocity of the bubble is independent of the bubble radius and also that the scaling of the velocity failed for $M > 2$.

The experiments of Layes et al. (2003) have been simulated numerically by Giordano & Burtschell (2006) and Layes & LeMétayer (2007), and both displayed good agreement with the experiments. The numerical schlieren image of a krypton bubble accelerated by an $M = 1.7$ shock showed a small secondary vortex ring at the apex of the bubble (Giordano & Burtschell 2006). Giordano & Burtschell also presented an analytical approach to evaluate the final volume of the inhomogeneity after the shock interaction. Numerically, extensive work has been done to study the shock-cylinder interaction. The experiments of Haas & Sturtevant have been simulated recently by Marquina & Mulet (2003), using very high spatial resolution, showing the growth of distinctive turbulent features in the flow field at late times.

Greenough & Jacobs (1996) implemented a high-order Godunov method in an adaptive mesh refinement environment to study this problem and successfully resolved many of the fine-scale details of the complex, highly vortical flow field observed in Jacobs's (1993) experiments. Bagabir & Drikakis (2001) studied the influence of incident shock strength on the cylindrical behavior with the same geometrical characteristics as Haas & Sturtevant's experiments.

As computational resources have improved dramatically over the past two decades, the capability has arisen to simulate SBIs numerically in three spatial dimensions at adequate grid resolution. As certain fundamental aspects of the flow-field evolution in SBIs are inherently 3D, particularly at high Mach numbers and Atwood numbers, such simulations have proven important. However, the scope of numerical work on 3D SBIs has been limited. Results from the first fully 3D simulations for SBIs were presented by Stone & Norman (1992). Their simulations were performed at a modest spatial resolution of R_{60} and indicated that vortex rings forming in SBIs within astrophysical contexts at $M \sim 10$ are unstable in three dimensions and tend to disintegrate into fragments at late times. Their figure 2 (Stone & Norman 1992) shows 3D-rendered images of the vorticity distribution in these high-M SBIs.

The work of Klein et al. (2003) includes a 3D adaptive mesh refinement simulation for the interaction of an $M \sim 10$ shock wave with a solid copper sphere in a low-density foam medium. This simulation showed that an azimuthal bending-mode instability similar to the Widnall instability for incompressible flows (Widnall et al. 1974) acts to break up the primary vortex ring generated in the SBI. This azimuthal redistribution of the sphere mass accounted for features of the experimental data that could not be fully explained by 2D simulations. This is depicted clearly in their figure 19 (Klein et al. 2003), which shows a 3D-rendered image of the multimode fluted azimuthal structure appearing on the shocked sphere at late times. The most comprehensive study of SBIs (across a wide range of Mach numbers and Atwood numbers) was performed by Niederhaus (2007) using a series of 3D multifluid Eulerian simulations. This work includes a detailed analysis of various integral features of the SBI, and it was shown that, although this problem exhibits a complex flow field, features such as mean density and bubble velocity can be scaled over a wide range of M for a fixed A using quantities calculated from 1D gas dynamics. Notable differences from the typical SBI morphology have been reported recently by Niederhaus et al. (2008) and Ranjan et al. (2008b) for scenarios with $M > 2$ and $A > 0.5$. In these scenarios the flow field mostly contains a diffuse turbulent plume (see **Figure 11**) at late times rather than coherent distinct vortex rings and vortex projectiles.

A heuristic model based on 1D gas dynamics for the circulation was presented by Niederhaus et al. (2008):

$$\Gamma_{1D} = u'_1 y_1 + \frac{D}{6}\left(u'_1 - u'_2\right)\left(\frac{-2y_1}{D}\right)^3 + u'_2\left(W_t - u'_2\right)\left(\frac{D}{\tilde{W}}\right) - u'_1\left(W_i + \frac{W_r}{\sqrt{M_r}}\right)\left(\frac{D}{\tilde{W}}\right). \quad (20)$$
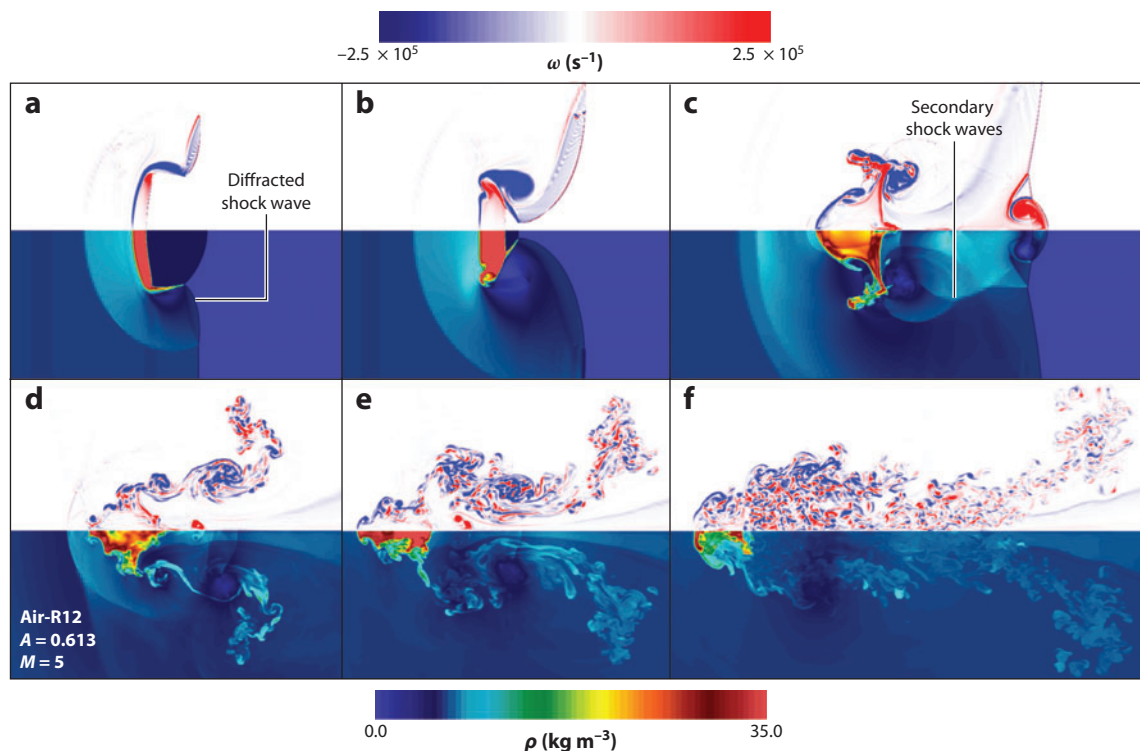
Figure 11

Density (*bottom panels*) and vorticity magnitude (*top panels*) for the $M = 5.0$ air-R12 scenario ($A = 0.613$): (*a*) $\tau = 1.5$, (*b*) $\tau = 2.5$, (*c*) $\tau = 5.0$, (*d*) $\tau = 10.1$, (*e*) $\tau = 15.0$, and (*f*) $\tau = 25.0$. The density color palette is shown at the bottom, and vorticity is plotted on a symmetric color palette centered on white, shown at the top. Note that $\tau = tW_i/R$ here. Incident shock-wave propagation is left to right. Figure taken from Niederhaus (2007).

The distance, on the bubble axis, from the bubble apex to the reflected shock wave is

$$y_1 = \frac{D}{\tilde{W}\sqrt{M_r}}\,(u_2' + W_r),\qquad(21)$$

and the effective shock-wave speed $\tilde{W}$ is the one defined by Zabusky & Zeng (1998). The circulation results from the 3D simulations compared with the model values Γ_{SZ}, Γ_{YKZ}, Γ_{PB}, and Γ_{1D}, and the Γ_{1D} model provided best agreement across the broad range of Mach numbers and density ratios considered. In the absence of 3D simulation data for circulation, Γ_{1D} is recommended as a best first estimate.

5. OTHER PHYSICAL SETTINGS

In physical scenarios of practical value, one frequently observes the interaction between a shock wave and flame front. As discussed above, Markstein (1957b) showed how combustion enhancement followed the acceleration of an initially curved flame surface by a shock wave. More recently, similar experimental studies performed by Thomas et al. (2001) have confirmed the deflagration-to-detonation transition following a shock-flame interaction in ethylene-air mixtures for a range of incident Mach numbers ($1.5 < M < 2.5$). The incident and reflected shock waves quickly

transition the initially laminar flame front to a turbulent front, drastically increasing the surface area and energy release rates. Although this study emphasized the shock-flame interaction, it only hinted at Mach number effects on the coupling between the hydrodynamics and chemistry. Later investigations (Dong et al. 2008, 2009; Gui et al. 2009) have started to consider Mach number effects, in addition to chemical reactivity, on the shock-flame interactions. Dong et al. (2009) looked at two Mach numbers ($M = 1.1$ and 2.1) and two different methane-air mixtures ($CH_4 + 2O_2 + 7.52N_2$ and $CH_4 + 2O_2 + 2.86N_2$) for shock-flame interactions. They found that for weak incident shock waves, the deformation of the spherical flame inhomogeneity develops similarly to an inert gas, suggesting that the chemical heat release does not play a major role in the development. For high incident Mach number, multiple Richtmyer-Meshkov instabilities lead to a highly distorted and turbulent flame compared with lower Mach number; however, the hydrodynamic instability process is still the dominant mechanism within the shock-flame interaction. Only for high Mach number and a more reactive mixture did the chemical heat release begin to play a significant role. The distorted flame front expanded rapidly, leading to the enhancement of the combustion process. Other notable work in this area includes that of Picone et al. (1985), Batley et al. (1994), Khokhlov et al. (1999), and Gamezo et al. (2001).

SAIFs also arise in shock-mitigation and energy-transfer schemes in which foams and bubbly liquids are used to redistribute the impulse of shock waves as they interact with void regions in the medium of propagation (Ball & East 1999, Collins et al. 2005, Delale et al. 2005). In many of these schemes, bubble collapse and jetting phenomena (Dear et al. 1988) are of foremost importance. These are also of great concern in extracorporeal shock-wave lithotripsy, which is a standard treatment for renal stones, employing high-amplitude ultrasound pulses to destroy stones by focused pressure waves and cavitation erosion (Crum 1988, Delius et al. 1998, Eisenmenger 2001). The interaction of the lithotripter pulses with gas voids results in their deformation and collapse, often with very strong subsequent jetting and pressure-redistribution effects (Coleman & Saunders 1993, Field 1991, Jamaluddin et al. 2005).

6. FINAL REMARKS

The interaction of a planar shock wave with a cylindrical or spherical density inhomogeneity produces three fundamental processes (compression/acceleration, shock reflection/refraction, and baroclinic vorticity generation), which are actually tightly coupled together. Their effects include the initial distortion of the bubble and the formation of primary and secondary vortex pairs or vortex rings (depending on the 2D or 3D nature of the initial geometry). In turn, these vortices lead to mass stripping off the original bubble and mixing of the bubble and ambient fluids. Even in this simplest configuration of a single curved inhomogeneity accelerated by a planar shock wave, the resulting flow exhibits a broad range of complicated features, from the reverberating wave field to the onset of turbulent mixing. The two fundamental parameters governing the interaction are the density contrast between the ambient and bubble gas and the strength of the accelerating shock. This kind of flow has direct relevance to certain natural and manmade occurrences and can also be used as a fundamental tool in the study of even more complicated situations in which a shock wave interacts with a whole field of acoustic impedance inhomogeneities. Significant progress has been made over the past 20 years, especially in the measurement and prediction of macroscopic geometrical, kinematic, and integral properties and in the development of dimensionless scaling laws between these properties and the flow-governing parameters. Currently open issues in the study of SBIs include the measurement and prediction of entire fields (velocity, density, pressure) and the coupling of other physics (chemical reactions, plasma physics) with the fluid dynamics described in this review.

DISCLOSURE STATEMENT

The authors are not aware of any affiliations, memberships, funding, or financial holdings that might be perceived as affecting the objectivity of this review.

ACKNOWLEDGMENTS

LITERATURE CITED

Anderson JD. 2003. *Modern Compressible Flow with Historical Perspective*. New York: McGraw-Hill. 3rd ed.

Arnett D. 2000. The role of mixing in astrophysics. *Astrophys. J. Suppl.* 127:213–17

Bagabir A, Drikakis D. 2001. Mach number effects on shock-bubble interaction. *Shock Waves* 11:209–18

Ball GJ, East RA. 1999. Shock and blast attenuation by aqueous foam barriers: influence of barrier geometry. *Shock Waves* 9:37–47

Baltrusaitis RM, Gittings ML, Weaver RP, Benjamin RF, Budzinski JM. 1996. Simulations of shock-generated instabilities. *Phys. Fluids* 8:2471–83

Batley GA, McIntosh AC, Brindley J, Falle SAEG. 1994. A numerical study of the vorticity field generated by the baroclinic effect due to the propagation of a planar pressure wave through a cylindrical premixed laminar flame. *J. Fluid Mech.* 279:217–37

Brouillette M. 2002. The Richtmyer-Meshkov instablity. *Annu. Rev. Fluid Mech.* 34:445–68

Budzinski JM, Benjamin RF, Jacobs JW. 1994. Influence of initial conditions on the flow patterns of a shock-accelerated thin fluid layer. *Phys. Fluids* 6:3510–12

Coleman AJ, Saunders JE. 1993. A review of the physical properties and biological effects of the high-amplitude acoustic fields used in extracorporeal lithotripsy. *Ultrasonics* 31:75–89

Collins TJB, Poludnenko A, Cunningham A, Frank A. 2005. Shock propagation in deuterium-tritium-saturated foam. *Phys. Plasmas* 12:062705

Cowperthwaite N. 1989. The interaction of a plane shock and a dense spherical inhomogeneity. *Physica D* 37:264–69

Crum LA. 1988. Cavitation microjets as a contributory mechanism for renal calculi disintegration in ESWL. *J. Urol.* 140:1587–90

Davy BA, Blackstock DT. 1971. Measurements of the refraction and diffraction of a short N wave by a gas-filled soap bubble. *J. Acoust. Soc. Am.* 49:732–37

Dear JP, Field JE, Walton AJ. 1988. Gas compression and jet formation in cavities collapsed by a shock wave. *Nature* 332:505–8

Delale CF, Nas S, Tryggvason G. 2005. Direct numerical simulations of shock propagation in bubbly liquids. *Phys. Fluids* 17:121705

Delius M, Ueberle F, Eisenmenger W. 1998. Extracorporeal shock waves act by shock wave-gas bubble interaction. *Ultrasound Med. Biol.* 24:1055–59

Dimotakis PE, Samtaney R. 2006. Planar shock cylindrical focusing by a perfect-gas lens. *Phys. Fluids* 18:031705

Dong G, Fan BC, Gui M, Li B. 2009. Numerical simulations of interactions between a flame bubble with an incident shock wave and its focusing wave. *J. Mech. Eng. Sci.* 223:2357–67

Dong G, Fan BC, Ye JF. 2008. Numerical investigation of ethylene flame bubble instability induced by shock waves. *Shock Waves* 17:409–19

Eisenmenger W. 2001. The mechanisms of stone fragmentation in ESWL. *Ultrasound Med. Biol.* 27:683–93

Field JE. 1991. The physics of liquid impact, shock wave interactions with cavities, and the implications to shock wave lithotripsy. *Phys. Med. Biol.* 36:1475–84

Reviews the various experimental techniques and their applications in understanding shock-accelerated flows.

Gamezo VN, Khokhlov AM, Oran ES. 2001. The influence of shock bifurcations on shock-flame interactions and DDT. *Combust. Flame* 126:1810–26

Giordano J, Burtschell Y. 2006. Richtmyer-Meshkov instability induced by shock-bubble interaction: numerical and analytical studies with experimental validation. *Phys. Fluids* 18:036102

Gracewski SM, Dahake G, Ding Z, Burns SJ, Everbach EC. 1993. Internal stress wave measurements in solid subjected to lithotripter pulses. *J. Acoust. Soc. Am.* 94:652–61

Greenough JA, Jacobs JW. 1996. A numerical study of shock-accelleration of a diffuse helium cylinder. In *Proc. 5th Int. Workshop Compressible Turbul. Mixing*, ed. R Young, J Glimm, B Boston, pp. 338–45. Singapore: World Sci.

Gui M, Fan B, Dong G, Ye J. 2009. Interaction of a reflected shock from a concave wall with a flame distorted by an incident shock. *Shock Waves* 18:487–94

Haas JF, Sturtevant B. 1987. Interaction of weak shock waves with cylindrical and spherical inhomogeneities. *J. Fluid Mech.* 181:41–76

Hansen JF, Robey HF, Klein RI, Miles AR. 2007. Experiment on the mass-stripping of an interstellar cloud in a high Mach number post-shock flow. *Phys. Plasmas* 14:056505

Henderson LF. 1989. On the refraction of shock waves. *J. Fluid Mech.* 198:365–86

Henderson LF, Colella P, Puckett EG. 1991. On the refraction of shock waves at a slow-fast gas interface. *J. Fluid Mech.* 224:1–27

Hwang U, Flanagan KA, Petre R. 2005. CHANDRA X-ray observation of a mature cloud-shock interaction in the bright eastern knot region of Puppis A. *Astrophys. J.* 635:355–64

Jacobs JW. 1992. Shock-induced mixing of a light-gas cylinder. *J. Fluid Mech.* 234:629–49

Jacobs JW. 1993. The dynamics of shock accelerated light and heavy gas cylinders. *Phys. Fluids A* 5:2239–47

Jacobs JW, Klein DL, Jenkins DG, Benjamin RF. 1993. Instability growth patterns of a shock-accelerated thin fluid layer. *Phys. Rev. Lett.* 70:583–86

Jamaluddin AR, Ball GJ, Leighton TJ. 2005. Free-Lagrange simulations of shock/bubble interaction in shock wave lithotripsy. In *Shock Waves: Proc. 24th Int. Symp. Shock Waves*, ed. ZL Jiang, pp. 1211–16. Berlin: Springer

Khokhlov AM, Oran ES, Thomas GO. 1999. Numerical simulation of deflagration-to-detonation transition: the role of shock-flame interactions in turbulent flame. *Combust. Flame* 117:323–39

Klein RI, Budil KS, Perry TS, Bach DR. 2000. Interaction of supernova remnants with interstellar clouds: from the NOVA laser to the galaxy. *Astrophys. J. Suppl.* 127:379–83

Klein RI, Budil KS, Perry TS, Bach DR. 2003. The interaction of supernova remnants with interstellar clouds: experiments on the NOVA laser. *Astrophys. J.* 583:245–59

Klein RI, McKee CF, Colella P. 1994. On the hydrodynamic interaction of shock waves with interstellar clouds. I. Nonradiative shocks in small clouds. *Astrophys. J.* 420:213–36

Kumar S, Orlicz G, Tomkins C, Goodenough C, Prestridge K, et al. 2005. Stretching of material lines in shock-accelerated gaseous flows. *Phys. Fluids* 17:082107

Kumar S, Vorobieff P, Orlicz G, Palekar A, Tomkins C, et al. 2007. Complex flow morphologies in shock-accelerated gaseous flows. *Physica D* 235:21–28

Lamb H. 1945. *Hydrodynamics*. New York: Dover

Layes G. 2005. *Etude expérimentale de l'interaction d'une onde de choc avec une bulle de gaz*. PhD thesis. Univ. Provence (Aix-Marseille I)

Layes G, Jourdan G, Houas L. 2003. Distortion of a spherical gaseous interface accelerated by a plane shock wave. *Phys. Rev. Lett.* 91:174502

Layes G, Jourdan G, Houas L. 2005. Experimental investigation of the shock wave interaction with a spherical gas inhomogeneity. *Phys. Fluids* 17:028103

Layes G, Jourdan G, Houas L. 2009. Experimental study on a plane shock wave accelerating a gas bubble. *Phys. Fluids* 21:074102

Layes G, LeMétayer O. 2007. Quantitative numerical and experimental studies of the shock accelerated heterogeneous bubbles motion. *Phys. Fluids* 19:042105

Levy K, Sadot O, Rikanati A, Kartoon D, Srebro Y, et al. 2003. Scaling in the shock-bubble interaction. *Laser Part. Beams* 21:335–39

Liepmann HW, Roshko A. 1957. *Elements of Gasdynamics*. New York: Wiley & Sons

Lindl J. 1995. Development of the indirect-drive approach to inertial confinement fusion and the target physics basis for ignition and gain. *Phys. Plasmas* 2:3933–4024

Lindl JD, McCrory RL, Campbell EM. 1992. Progress toward ignition and burn propagation in inertial confinement fusion. *Phys. Today* 45:32–40

Marble FE, Zukoski EE, Jacobs J, Hendricks G, Waitz I. 1990. Shock enhancement and control of hypersonic mixing and combustion. In *26th AIAA, SAE, ASME, and ASEE Joint Propul. Conf., Orlando*, ed. KM Isaac, A Missoum

Markstein GH. 1957a. Flow disturbances induced near a slightly wavy contact surface, or flame front, traversed by a shock wave. *J. Aeronaut. Sci.* 24:238–39

Markstein GH. 1957b. A shock tube study of the flame front-pressure wave interaction. In *6th Int. Symp. Combust.*, pp. 387–98. New York: Reinhold

Marquina A, Mulet P. 2003. A flux-split algorithm applied to conservative models for multicomponent compressible flows. *J. Comput. Phys.* 185:120–38

Niederhaus JHJ. 2007. *A computational parameter study for three-dimensional shock-bubble interactions*. PhD thesis. Univ. Wisconsin, Madison

Niederhaus JHJ, Greenough JA, Oakley JG, Ranjan D, Anderson MH, Bonazza R. 2008. A computational parameter study for the three-dimensional shock-bubble interaction. *J. Fluid Mech.* 594:85–124

Picone JM, Boris JP. 1988. Vorticity generation by shock propagation through bubbles in a gas. *J. Fluid Mech.* 189:23–51

Picone JM, Oran ES, Boris JP, Young TR Jr. 1985. Theory of voriticty generation by shock wave and flame interactions. In *Dynamics of Shock Waves, Explosions, and Detonations*, ed. JR Bowen, N Manson, AK Oppenheim, RI Soloukhin, pp. 429–48. Prog. Astronaut. Aeronaut. Vol. 94. New York: AIAA

Prestridge K, Vorobieff P, Rightley PM, Benjamin RF. 2001. Validation of an instability growth model using particle image velocimetry measurements. *Phys. Rev. Lett.* 84:4353–56

Quirk JJ, Karni S. 1996. On the dynamics of a shock-bubble interaction. *J. Fluid Mech.* 318:129–63

Ranjan D. 2007. *Experimental investigation of the shock-induced distortion of a spherical gas inhomogeneity*. PhD thesis. Univ. Wisconsin, Madison

Ranjan D, Anderson M, Oakley J, Bonazza R. 2005. Experimental investigation of a strongly shocked gas bubble. *Phys. Rev. Lett.* 94:184507

Ranjan D, Niederhaus J, Motl B, Anderson M, Oakley J, Bonazza R. 2007. Experimental investigation of primary and secondary features in high-Mach-number shock-bubble interaction. *Phys. Rev. Lett.* 98:024502

Ranjan D, Niederhaus JHJ, Oakley JG, Anderson MH, Bonazza R, Greenough JA. 2008a. Shock-bubble interactions: features of divergent shock-refraction geometry observed in experiments and simulations. *Phys. Fluids* 20:036101

Ranjan D, Niederhaus JHJ, Oakley JG, Anderson MH, Greenough JA, Bonazza R. 2008b. Experimental and numerical investigation of shock-induced distortion of a spherical gas inhomogeneity. *Phys. Scr.* 2008:014020

Robey HF, Perry TS, Klein RI, Kane JO, Greenough JA, Boehly TR. 2002. Experimental investigation of the three-dimensional interaction of a strong shock with a spherical density inhomogeneity. *Phys. Rev. Lett.* 89:085001

Rudinger G. 1958. Shock wave and flame interactions. In *Combustions and Propulsion: Third AGARD Colloquium*, ed. MW Thring, pp. 153–82. New York: Pergamon

Rudinger G, Somers LM. 1960. Behavior of small regions of different gases carried in accelerated gas flows. *J. Fluid Mech.* 7:161–76

Samtaney R, Zabusky NJ. 1994. Circulation deposition on shock-accelerated planar and curved density-stratified interfaces: models and scaling laws. *J. Fluid Mech.* 269:45–78

Stone JM, Norman ML. 1992. The three-dimensional interaction of a supernova remnant with an interstellar cloud. *Astrophys. J.* 390:L17–19

Taylor GI. 1953. Formation of a vortex ring by giving an impulse to a circular disk and then dissolving it away. *J. Appl. Phys.* 24:104–5

First high Mach number experiments showing the presence of secondary vortex structures in the flow field.

Thomas G, Bambrey R, Brown C. 2001. Experimental observations of flame acceleration and transition to detonation following shock-flame interaction. *Combust. Theory Model.* 5:573–94

Thompson PA. 1984. *Compressible-Fluid Dynamics*. New York: McGraw-Hill

Tomkins C, Kumar S, Prestridge GOK. 2008. An experimental investigation of mixing mechanisms in shock-accelerated flow. *J. Fluid Mech.* 611:131–50

Tomkins C, Prestridge K, Rightley P, Marr-Lyon M, Vorobieff P, Benjamin R. 2003. A quantitative study of the interaction of two Richtmyer-Meshkov-unstable gas cylinders. *Phys. Fluids* 15:986–1004

Widnall SE, Bliss DB, Tsai CY. 1974. The instability of short waves on a vortex ring. *J. Fluid Mech.* 66:35–47

Winkler KH, Chalmers JW, Hodson SW, Woodward PR, Zabusky NJ. 1987. A numerical laboratory. *Phys. Today* 40:28–37

Yang J, Kubota T, Zukoski EE. 1993. Applications of shock-induced mixing to supersonic combustion. *AIAA J.* 31:854–62

Yang J, Kubota T, Zukoski EE. 1994. A model for characterization of a vortex pair formed by shock passage over a light-gas inhomogeneity. *J. Fluid Mech.* 258:217–44

Zabusky NJ. 1999. Vortex paradigm for accelerated inhomogeneous flows: visiometrics for the Rayleigh-Taylor and Richtmyer-Meshkov environments. *Annu. Rev. Fluid Mech.* 31:495–536

Zabusky NJ, Zeng SM. 1998. Shock cavity implosion morphologies and vortical projectile generation in axisymmetric shock-spherical fast/slow bubble interactions. *J. Fluid Mech.* 362:327–46

Reviews the application of the vortex paradigm to shock-accelerated flows.

Contents

Indexes

Errata

An online log of corrections to *Annual Review of Fluid Mechanics* articles may be found
at http://fluid.annualreviews.org/errata.shtml